

Summary of AFIN measurements on Atka Bay land-fast sea ice in 2013

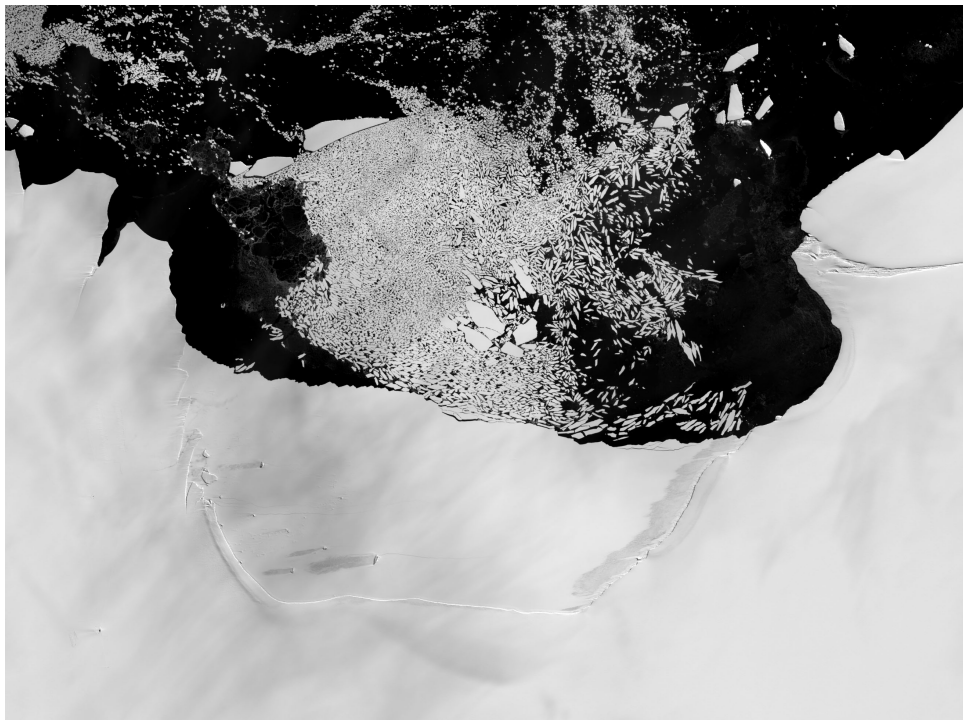
- Field report -

Mario Hoppmann, Marcel Nicolaus, Lisa-Katharina Behrens, Julia Regnery

Contact:

Mario.Hoppmann@awi.de,

Marcel.Nicolaus@awi.de



Alfred-Wegener-Institut Helmholtz-Zentrum für Polar- und Meeresforschung

Am Handelshafen 12, 27570 Bremerhaven, Germany

- 26 May 2014 -

Table of Contents

1	Sea-ice conditions	3
1.1	Sea-ice growth history	3
1.2	Sea-ice thickness and snow depth	3
1.3	Sub-ice platelet layer	4
1.4	Sea-ice breakout	7
2	EM31 thickness transects	9
3	Automatic weather station	14
4	Radiation station	18
4.1	06 September to 11 September 2013	18
4.2	29 September 2013 to 03 January 2014	19
5	Sea-ice mass balance buoy	23
6	Snow buoys	24
A	Acknowledgements	29

1. Sea-ice conditions

1.1. Sea-ice growth history

In 2013, the fast-ice cover of Atka Bay consisted exclusively of thick sea ice grown in the previous year. The large iceberg B15G, which grounded in front of Atka Bay in September 2012, prevented fast-ice destabilization and subsequent breakout at the beginning of 2013. This situation was in strong contrast to recent years, when an initial breakout occurred as early as December. Therefore, the sea-ice conditions in 2013 were strongly similar to those in 2012. Figure 1 provides an overview of the variable sea-ice regimes as observed in November 2012.

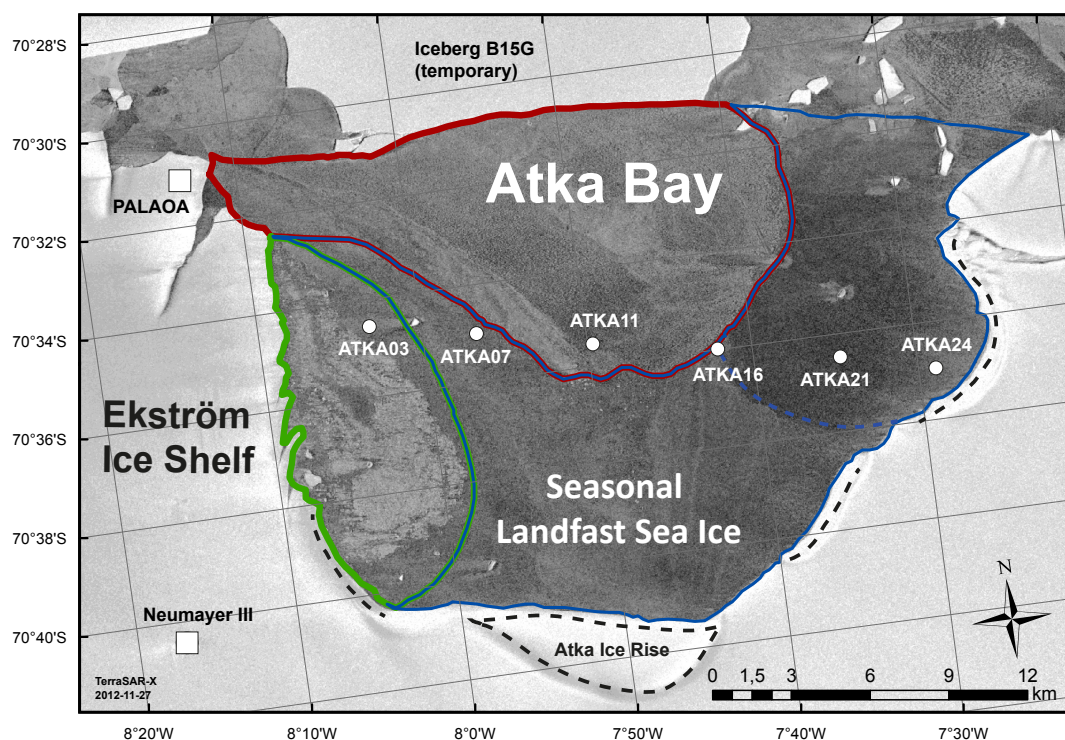


Figure 1: Overview of variable sea-ice conditions at Atka Bay in 2012, and consequently also in 2013. An area of pressure-ridged sea ice formed in March/April 2012 (green), level sea ice formed between April and June 2012 (blue) and level sea ice formed in October 2012 (red) were observed.

1.2. Sea-ice thickness and snow depth

Sea-ice thickness, snow depth and freeboard were measured regularly at six study sites between 07 January 2013 and 17 January 2014. We also performed measurements of platelet-layer thickness by the metal-bar method. Auxiliary measurements included air-, surface- and snow/ice-interface temperatures. Photos were taken in four directions during each sampling. The locations of these measurements were the same as in 2011 and 2012 for consistency reasons (Figure 1, Table 1).

Results of sea-ice thickness, snow depth and freeboard measurements are shown in Figure 2.

Table 1: Study sites in 2013. Abbr.: D: deformed ice; L: level ice;

Study Site	Latitude (S)	Longitude (W)	Ice type
ATKA03	70° 34.513'	8° 02.961'	D
ATKA07	70° 34.995'	7° 56.732'	D
ATKA11	70° 35.530'	7° 49.485'	L
ATKA16	70° 35.988'	7° 42.095'	D
ATKA21	70° 36.471'	7° 34.610'	L
ATKA24	70° 36.955'	7° 28.965'	L

Thickness of the fast ice was high at all sites, because of its age and the absence of bottom melt during summer 2012/13. The age of the sea ice also had an impact on the snow cover, which was substantial also due to the minor occurrence of surface melt during summer 2012/13. For these reasons, only one drilling was conducted per visit and site. Sometimes, an accurate freeboard measurement was not possible due to the high snow load and platelets additionally obstructing the measurement. Quick refreezing of the drill-hole was also an issue.

Sea-ice thickness was >2 m at nearly all sites already in April 2013. Only ATKA11 had a lower thickness because of an intermediate breakout in August 2012. At the end of the growth season, sea-ice thickness ranged from 2.5 (ATKA21) to 4 m (ATKA03). Due to the low number of measurements at each site, a high local variability was not accounted for. Therefore the thickness evolution was not monotonically increasing in the data as expected during growth (e.g. ATKA07). Snow cover was generally increasing between January and November 2013, when a slight overall decline set in. This was likely due to enhanced melt during summer 2013/14, leading to a very wet and partly ponded surface (Figure 3).

Snow cover was lowest at ATKA03, where an iceberg heavily influenced the snow drift and deposition. Usually, snow depth in the west is highest due to redistribution by easterly winds. At ATKA24, the influence of the nearby ice-shelf edge prevented stronger snow deposition. The other sites exhibited a very thick snow cover, with extrema of nearly 2 m in November, also partly leading to negative freeboard despite the thick sea ice.

1.3. Sub-ice platelet layer

Results of platelet-layer thickness measurements are presented in Figure 4. The thickness of the sub-ice platelet layer was on average 3 m in January 2013. It slightly increased until the end of April 2013, which was most likely a result of platelet redistribution by currents directly under the sea ice, instead of new accumulation. In other years, a closed fast-ice cover had not even established in April, and platelet accumulation only took place from May/June onwards.

Platelet-layer thickness continuously increased at all sites between June and December. The average accumulation at all sites in 2013 was approximately 4 m, leading to a mean overall thickness of 7 m. The total thickness gain at ATKA11 was 6 m, which is probably also a

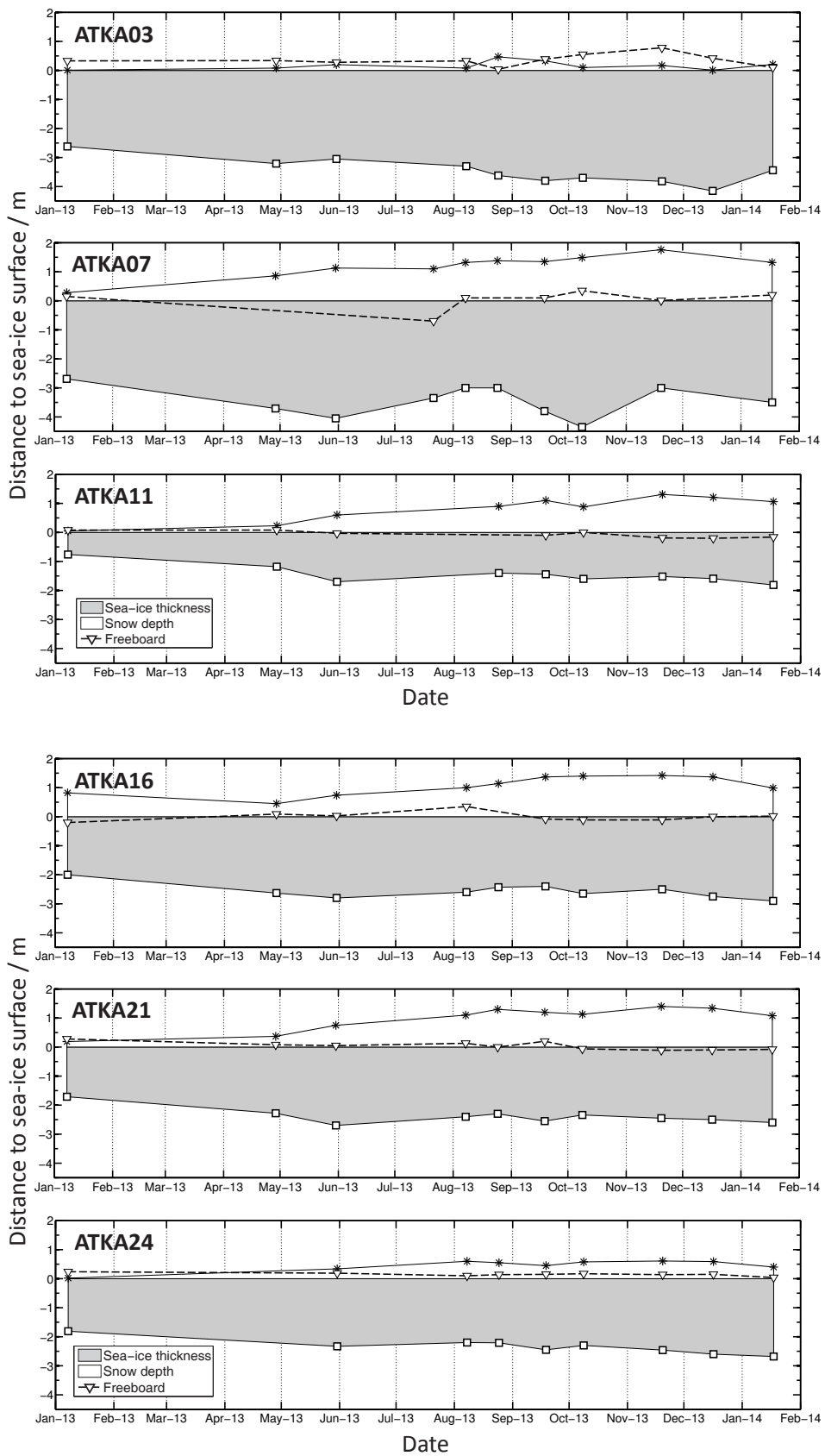


Figure 2: Sea-ice thickness, snow depth and freeboard at the six sampling sites between January 2013 and January 2014.



Figure 3: Wet and partly ponded surface near ATKA03 on 17 January 2014.

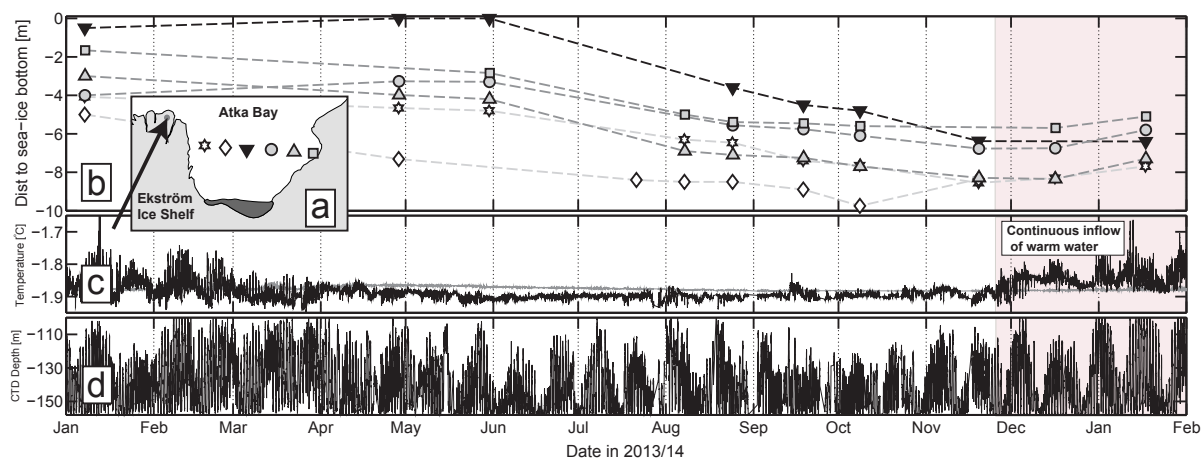


Figure 4: Platelet-layer thickness at the six sites in 2013/14, along with oceanographic conditions recorded at a measurement site below the Ekström Ice Shelf. a) Coarse map of the study area. Sampling sites are indicated by symbols (ATKA03: \star , ATKA07: \diamond , ATKA11: ∇ , ATKA16: \circ , ATKA21: \triangle , ATKA24: \square) and grouped into western, central and eastern sites. The location of the oceanographic measurements in c) and is indicated by the dot and the arrow. b) Sub-ice platelet-layer thickness evolution at the different study sites, with symbols corresponding to their location according to a). c) In-situ temperature (black) and corresponding surface freezing point (gray) of the water at a location below the northern Ekström Ice Shelf in 2013/14. The shaded area indicates the continuous inflow of warm water masses. d) Water depth of the corresponding temperature record.

result of platelet redistribution. This redistribution tendency is generally visible in the data when comparing the variable initial conditions with the nearly equal thicknesses at the end of the year. The seawater temperature in the ice-shelf cavity (Figure 4b) was below the surface freezing point between April and November 2013. With the continuous inflow of relatively warm water at the end of November 2013, the platelet-layer thickness started to decrease. The pressure data of the instrument shows a distinct 14-days tidal cycle (Figure 4c), which was most pronounced from April 2013.

1.4. Sea-ice breakout

Iceberg B15G broke off between 10 and 12 August 2013. It left behind several smaller grounded segments in the northwest. Unfortunately, no satellite imagery is available of this event. On 23 August 2013, it had traveled almost 200 km to the west (Figure 5). The fast-ice conditions at Atka Bay were generally unaffected by this event.

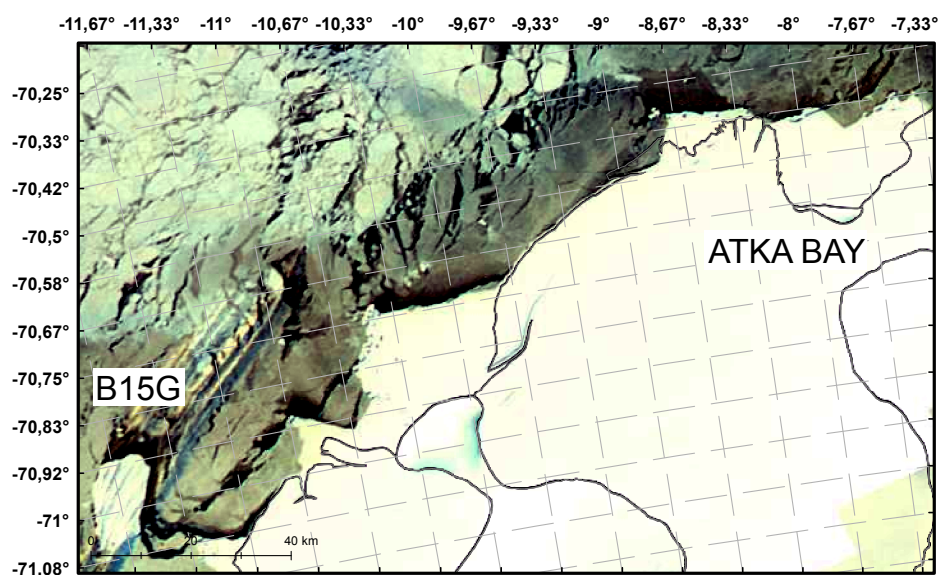


Figure 5: Map of the southeastern Weddell Sea (MODIS Terra, 23 August 2013).

With this natural barrier now gone, and the front of the Ekström Ice Shelf pack-ice free, the fast ice started to break out at the beginning of February 2014. As apparent from Landsat satellite imagery (Figure 6), the sea ice disintegrated evenly from north, mostly into floes smaller than 200 m. Sea ice covering about 1/3 of the total Atka Bay area remained in the south. Hence it is likely that a large fraction of the platelet layer also stayed under this remaining fast ice, potentially contributing to the bay-wide platelet layer thickness in 2014.

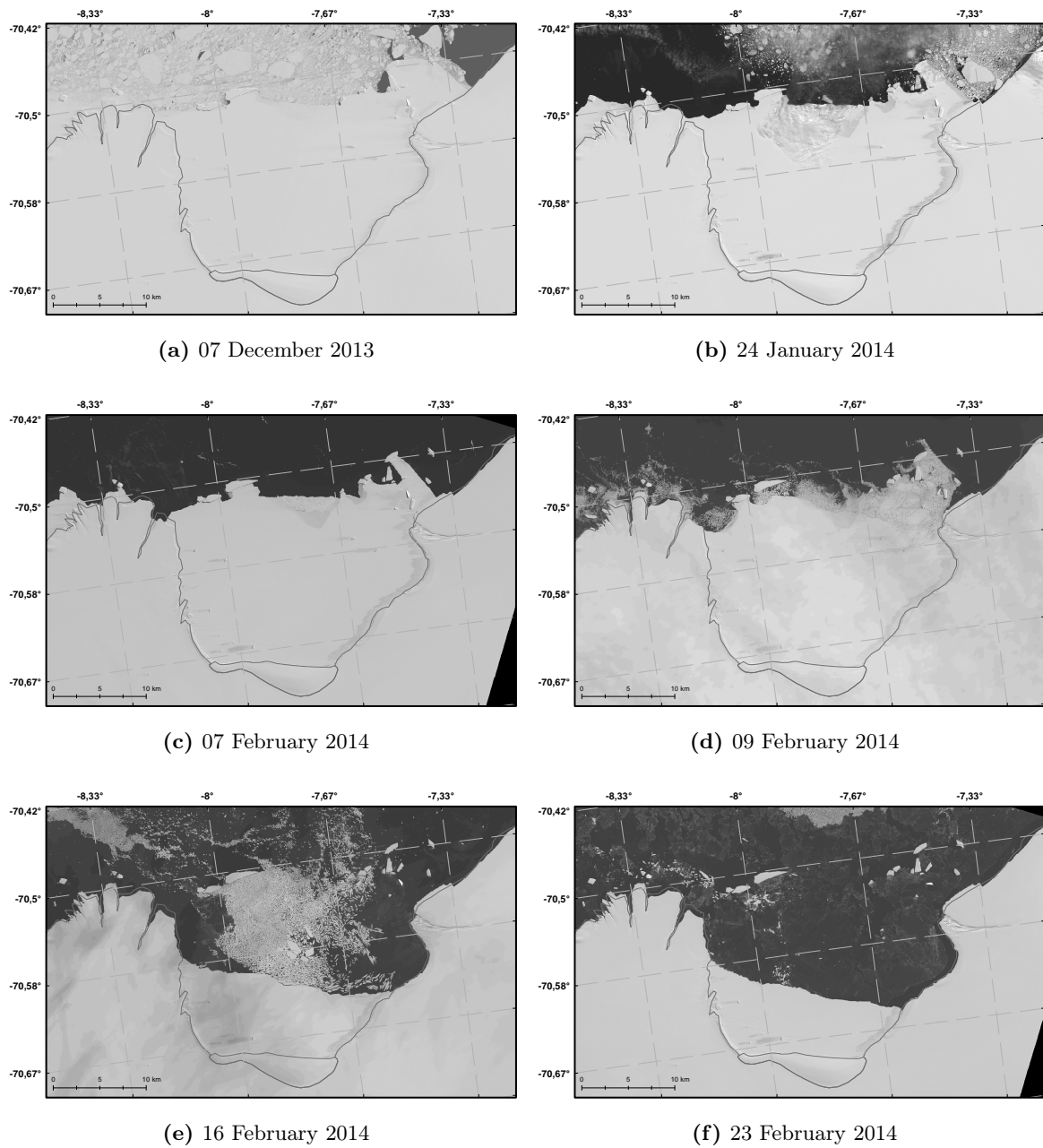


Figure 6: Landsat images depicting sea-ice breakout at Atka Bay

2. EM31 thickness transects

We conducted 8 electromagnetic induction sounding thickness surveys between 28 April 2013 and 17 January 2014, using a Geonics EM31 MKII. The instrument was mounted in a kayak in horizontal mode, and pulled behind a snowmobile. Conductivities were recorded by two dataloggers (Allegro MX and Archer), and positions were simultaneously acquired by at least 2 Garmin GPS. An additional modification of the power supply was necessary for the instrument to work at temperatures <25 °C. The instrument was calibrated at ATKA03 on 16 December 2013 and at ATKA24 on 05 January 2014. On both occasions, the EM31 was calibrated while mounted in the kayak. On 05 January, we also performed a calibration without the kayak. It became evident that the apparent conductivities between the calibrations with and without the kayak were different by a factor of three. Obviously the kayak seemed to shield the EM response from the receiver, an effect which was not expected. In addition, the calibrations in the kayak at different sites also yielded different exponential fits. The reasons for this behavior are currently unclear. One possible explanation would be potentially different conductivities of the platelet layer at different calibration sites. Furthermore, the reliability of the calibrations in the kayak are questionable, as the apparent conductivities were very low. This is attributed to the large distance of the instrument to the conductive layer. Data points for lower distances to the conductive layer could unfortunately not be recorded due to the lack of thinner sea ice. A calibration over open water was not considered useful due to the lack of platelets underneath (which modify the overall conductivity). At the same time, the calibration without the kayak was not considered useful as the EM31 is always mounted in the kayak during the thickness transects. Therefore, total thickness was calculated from apparent conductivities by a single exponential fit to the calibration data of 16 December 2013 (Figure 7) for all data presented here. The manual calibration curve roughly corresponds to a modeled curve with a seawater conductivity of 400 ms/m, which is very low. The exponential fit for the calibration of 05 January 2014 resulted in an even lower conductivity. Even for a platelet environment, a conductivity >1000 ms/m is expected. Hence, the uncertainty in the calculated total thickness may be very large, but is not quantified here.

The EM31 conductivities recorded by the Archer datalogger were aligned to the respective GPS position recorded by the Garmin GPS according to the timestamp. The data shown here were corrected for standing times of the instrument (for example during a drilling) through a GPS distance threshold of 0.5 m between two data points.

Figure 8 gives an overview of all EM31 transects obtained during 2013/14. The colorbar indicates sea-ice thickness plus snow depth, with a calibration according to Figure 7. The data of 28 April 2013 are not shown because the GPS track was not recorded. On 21 July 2013, the transect had to be aborted at ATKA07. We repeated the transects as accurate as possible to be able to better inter-compare the data. Therefore, additional thickness data was removed for the analysis. Snow-depth measurements were also performed along the transects, at an approximate spacing of 1 km (Table 2)

Table 2: Snow depth (m) during EM31 transects

Site/Date	28 Apr	21 Jul	07 Aug	23 Aug	18 Sep	08 Oct	19 Nov	16 Dec	17 Jan
Atka00	1.15	1.55	1.82	0.18	1.90	1.75	1.98	1.90	1.76
Atka01	0.55	1.32	0.98	1.33	1.32	1.32	1.37	1.47	1.74
Atka02	0.02	0.28	0.72	0.10	0.94	0.76	0.88	1.09	0.65
Atka03	0.25	0.08	0.10	0.18	0.08	0.12	0.14	0.00	0.10
Atka04	1.00	1.24	0.41	0.20	1.81	2.03	1.95	1.39	1.69
Atka05	0.49	1.48	0.13	0.05	1.60	1.39	1.93	2.13	1.96
Atka06	0.34	1.41	1.17	1.44	0.30	0.16	1.97	1.63	1.62
Atka07	0.98	0.68	1.46	1.24	1.53	1.68	1.87	1.63	1.52
Atka08	0.20		1.31	1.16	1.31	1.30	1.29	1.28	1.08
Atka09	0.35		1.12	1.08	1.30	1.29	1.35	1.35	1.48
Atka10	0.27		1.06	0.19	1.14	1.22	1.63	1.29	1.11
Atka11	0.24		0.96	0.89	1.16	1.04	1.19	1.27	0.94
Atka12	0.24		0.91	0.87	0.96	1.06	1.27	1.26	1.80
Atka13	0.36		1.00	0.91	1.18	1.29	1.18	1.17	0.85
Atka14	0.27		1.10	0.90	0.96	1.09	1.28	1.31	0.92
Atka15	0.17		0.93	0.92	0.89	0.95	1.29	1.29	0.84
Atka16	0.38		1.14	1.15	1.16	1.27	1.41	1.26	0.95
Atka17	0.11		1.01	0.96	1.58	1.14	1.38	1.08	1.22
Atka18			0.94	0.91	1.22	1.17	1.35	1.19	1.04
Atka19			0.95	1.01	1.01	0.95	1.31	1.27	1.16
Atka20			0.81	0.84	1.01	1.07	1.26	1.25	0.95
Atka21			1.18	1.17	1.39	1.27	1.42	1.41	1.25
Atka22			0.93	1.15	1.31	1.07	1.31	1.31	0.98
Atka23			0.91	0.82	0.95	0.97	1.23	1.21	1.18
Atka24			0.57	0.46	0.53	0.53	0.63	0.72	0.40
Mean	0.41	1.01	0.94	0.80	1.14	1.12	1.35	1.29	1.17
Std	0.32	0.58	0.37	0.42	0.42	0.42	0.42	0.38	0.45
Median	0.31	1.28	0.96	0.91	1.16	1.14	1.31	1.28	1.11

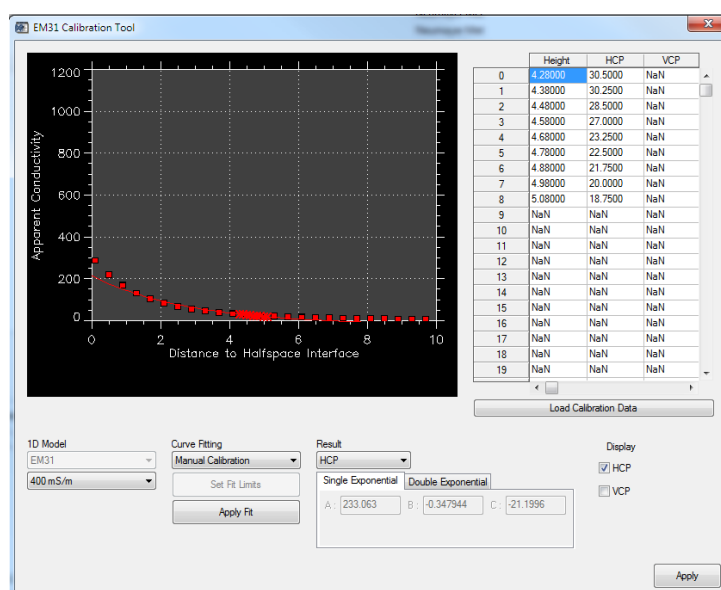


Figure 7: EM31 calibration on 16 December 2013. The red crosses are the data points from the calibration, the squares represent the 1-D exponential model best fitting to the data. The calibration coefficients for all data presented in this report are found in the lower box.

The difference between the sea-ice types according to Figure 1 is clearly visible in the thickness data. However, these maps are mainly shown as a help to interpret the total thickness distribution, which is more useful to investigate.

Figure 9 shows the corresponding total thickness distributions in normalized histograms (by area), and gives the mean and median of the data along with the standard deviation. The data for 28 April 2013 is included, but was not corrected for standing times of the instrument. The data from 21 July 2013 is biased towards higher thicknesses due to its limited coverage. A time series of statistical parameters is presented in Figure 10. The data from 21 July 2013 is omitted. Please note that the values for snow depth are only based on 24 measurements, and might not be entirely representative for the general snow conditions. Generally, an expected increase in total thickness is evident. Between April 2013 and January 2014, the total thickness gain is on the order of 2 m. This was mainly composed of sea-ice thermodynamic growth, snow precipitation and snow drift from the eastern ice shelf. According to sea-ice thickness data from drillings and a mass balance buoy (see below), the average sea-ice growth was on the order of 1 m in 2013. Snow precipitation and drift would then also amount for about 1 m, which also is supported by Table 2. In November and December 2013, thicknesses below 2 m rarely occurred. The width of the histogram (and thereby the standard deviation) then strongly increases in January 2014, again showing thicknesses as low as 1 m. This was most likely mainly a result of snow melt, and to a lesser degree sea-ice bottom melt. Due to the changing properties of the oceanic regime immediately below the fast ice, especially during melt of the platelet layer, the uncertainty of the presented EM data may be high.

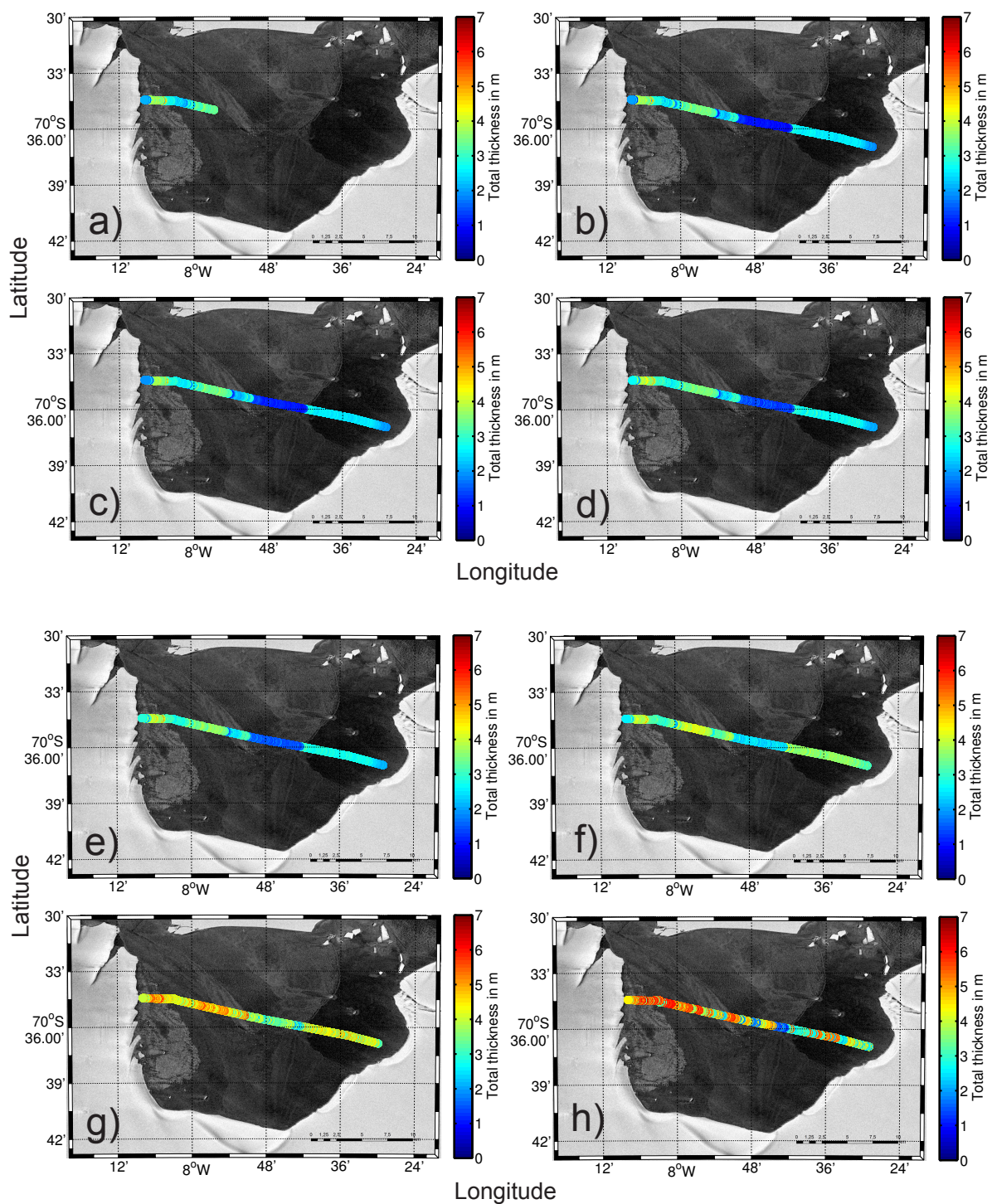


Figure 8: EM31 total thickness transects. a) 21 July, b) 07 August, c) 23 August, d) 18 September, e) 08 October, f) 19 November, g) 16 December 2013 and h) 17 January 2014.

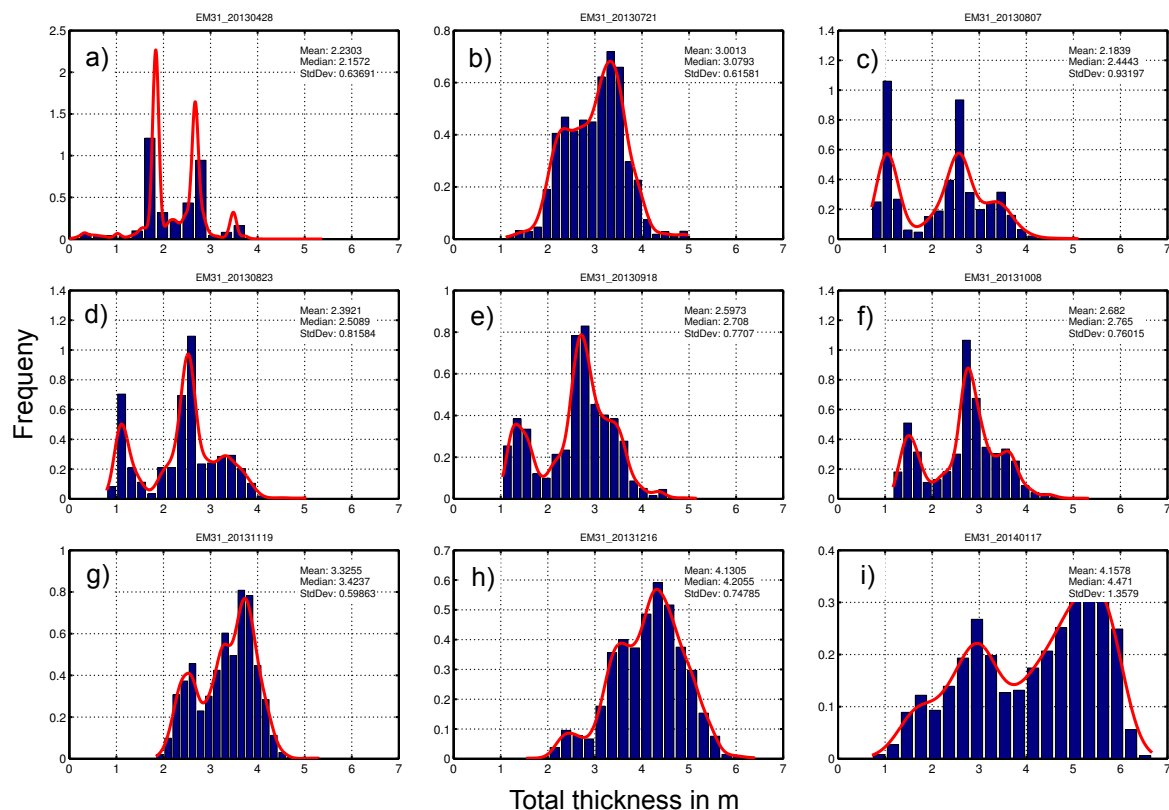


Figure 9: EM31 total thickness histograms. a) 28 April, b) 21 July, c) 07 August, d) 23 August, e) 18 September, f) 08 October, g) 19 November, h) 16 December 2013 and i) 17 January 2014.

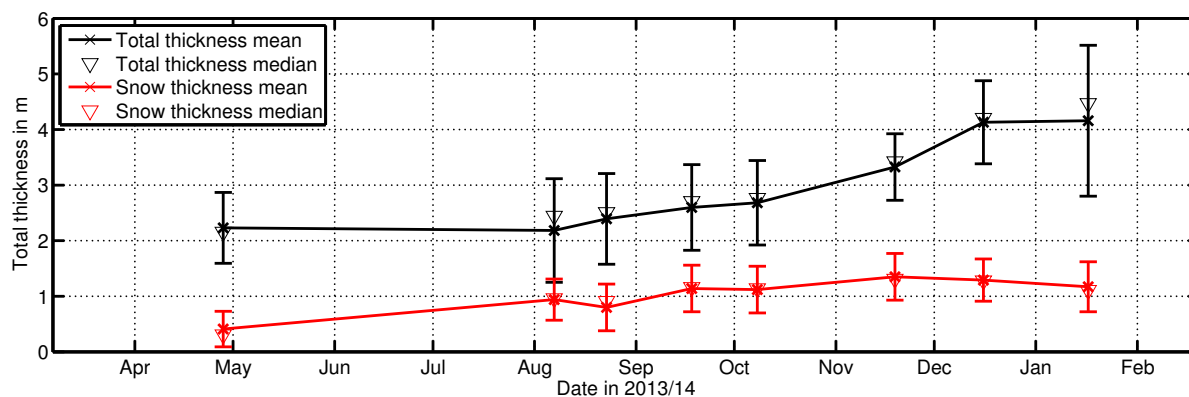


Figure 10: Time series of EM31 total thickness / snow depth statistical parameters. The error bars represent one standard deviation.

3. Automatic weather station

We deployed an automatic weather station (AWS) at ATKA03 on 30 May 2013. The AWS recorded air temperature, relative humidity, barometric pressure, wind speed/direction as well as downward and upward long- /shortwave radiation in 2 m height at 1 minute intervals. Refer to Table 3 for the instrumentation. The data was stored on a memory card. Additionally, we used a WLAN antenna to transfer the data directly to Neumayer III.

Table 3: Instrumentation and measured parameters of AWS

Instrument	Measured parameter
Temperature and Humidity Probe (shielded HMP155A, Vaisala)	Air temperature, relative humidity
Barometric Pressure Sensor (61302V, RM Young Company)	Barometric pressure
Marine Wind Monitor (05106-5, RM Young Company)	Wind direction, wind speed
Net Radiometer (CNR4, Kipp & Zonen)	Bulk long- and short-wavelength radiation
Sonic Ranging Sensor (SR50A, Campbell Scientific)	Snow height

Figure 11 shows the setup of autonomous measurements at ATKA03 in September. The radiation station and mass balance buoy (not shown) are described in more detail below.

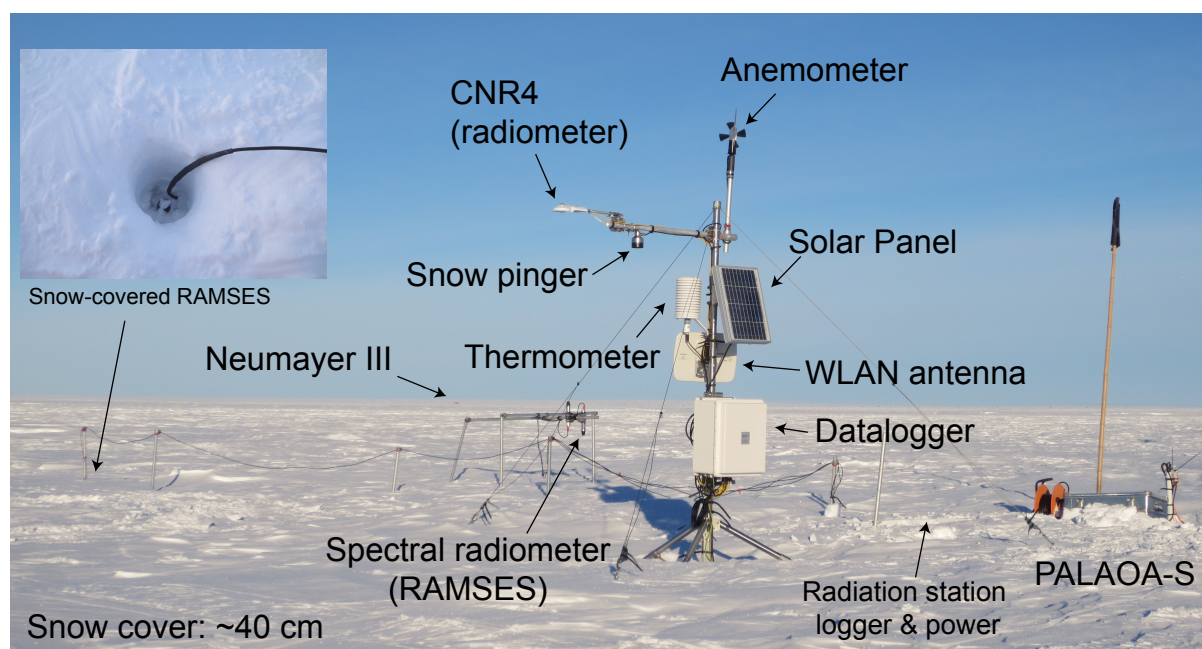


Figure 11: Setup of autonomous measurements at ATKA03 on 18 September 2013.

Atmospheric measurements recorded by the AWS are compared to data from the meteorolog-

ical observatory at Neumayer III in Figure 12. The average difference measured at both sites is calculated from daily means.

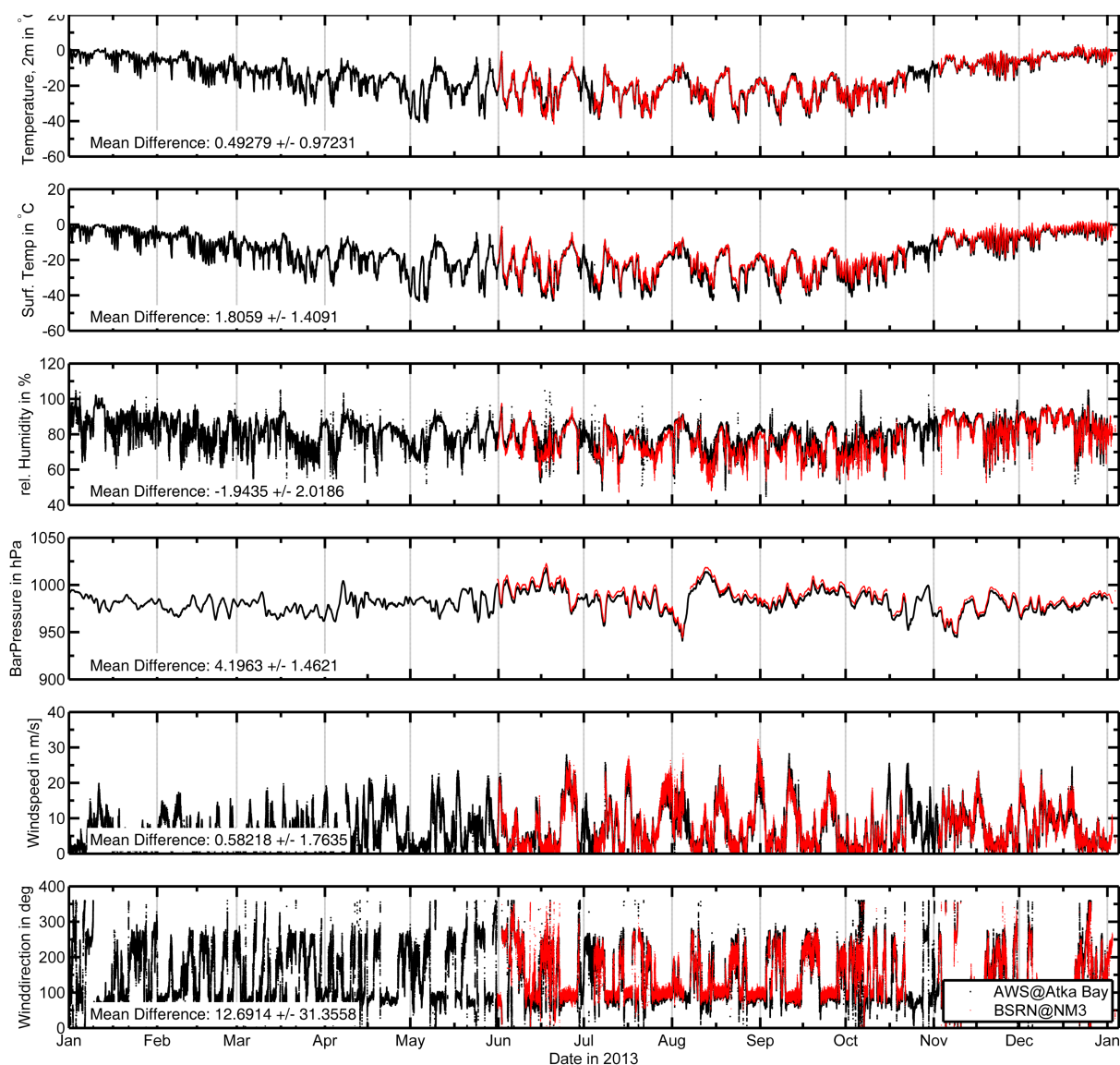


Figure 12: Meteorological measurements at Neumayer III (black) and on Atka Bay fast ice (red) in 2013. a) 2 m air temperature; b) surface temperature calculated from upward long-wavelength radiation; c) relative humidity; d) barometric pressure; e) windspeed; f) wind direction (from North).

Measurements of solar radiation recorded by the AWS are compared to data from the meteorological observatory at Neumayer III in Figure 13. The average difference measured at both sites is calculated from daily means.

An in-depth analysis of this data is out of the scope of this report. However, a few general remarks shall be made here. The air temperature directly on the sea ice was about 0.5 °C higher compared to Neumayer. The difference in barometric pressure between Neumayer (on the ice shelf) and the AWS (on the sea ice) originates from the height of the instruments. The

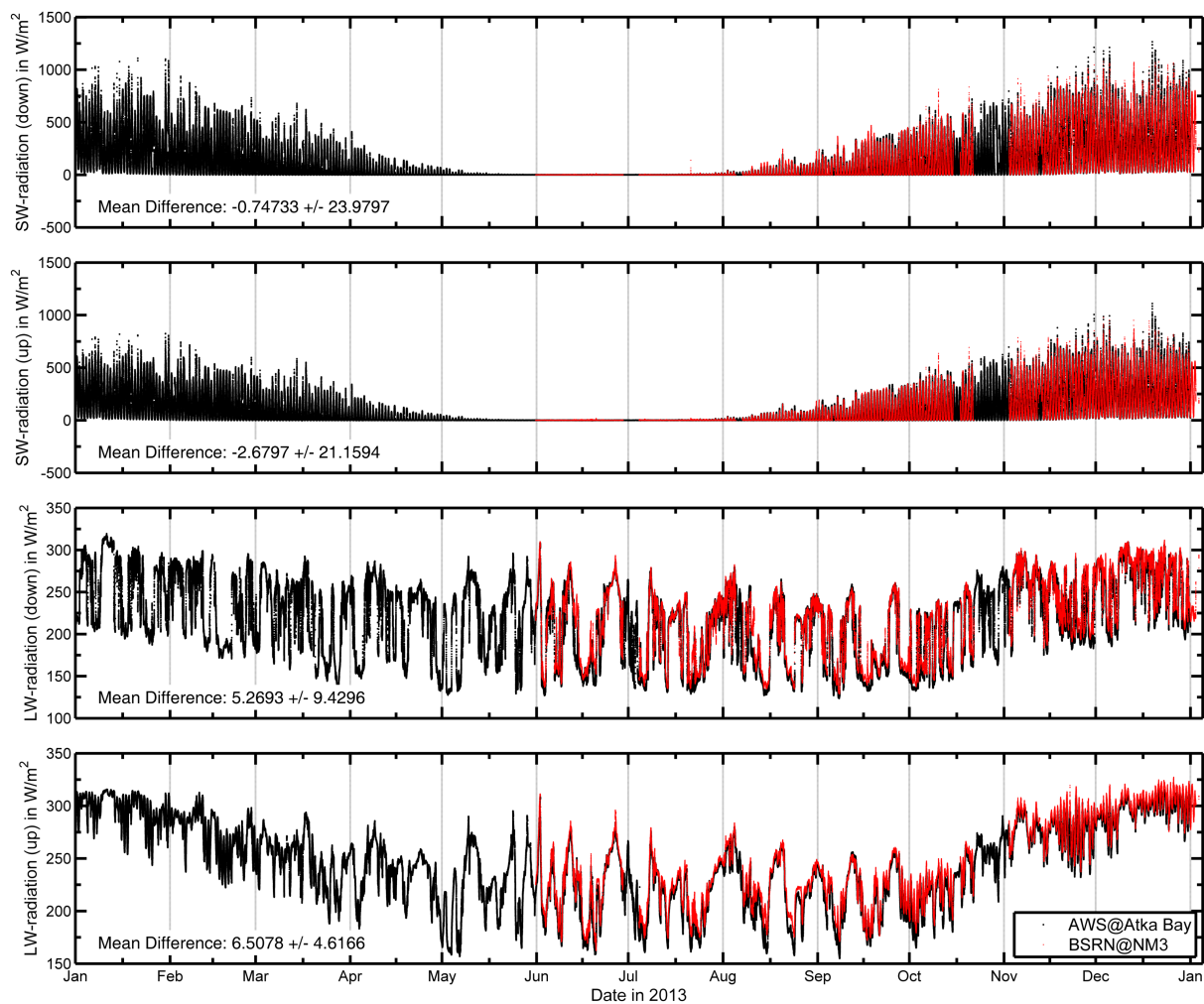


Figure 13: Radiation measurements at Neumayer III (black) and on Atka Bay fast ice (red) in 2013. a) Downward short-wavelength radiation (SWD); b) upward short-wavelength radiation (SWU); b) downward long-wavelength radiation (lwd); b) upward long-wavelength radiation (LWU);

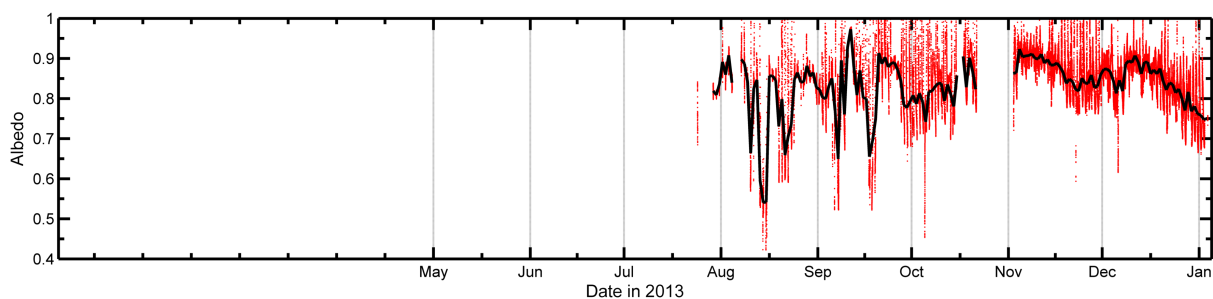


Figure 14: Albedo at ATKA03, calculated from down- and upward long-wave radiation. The daily average is shown in black.

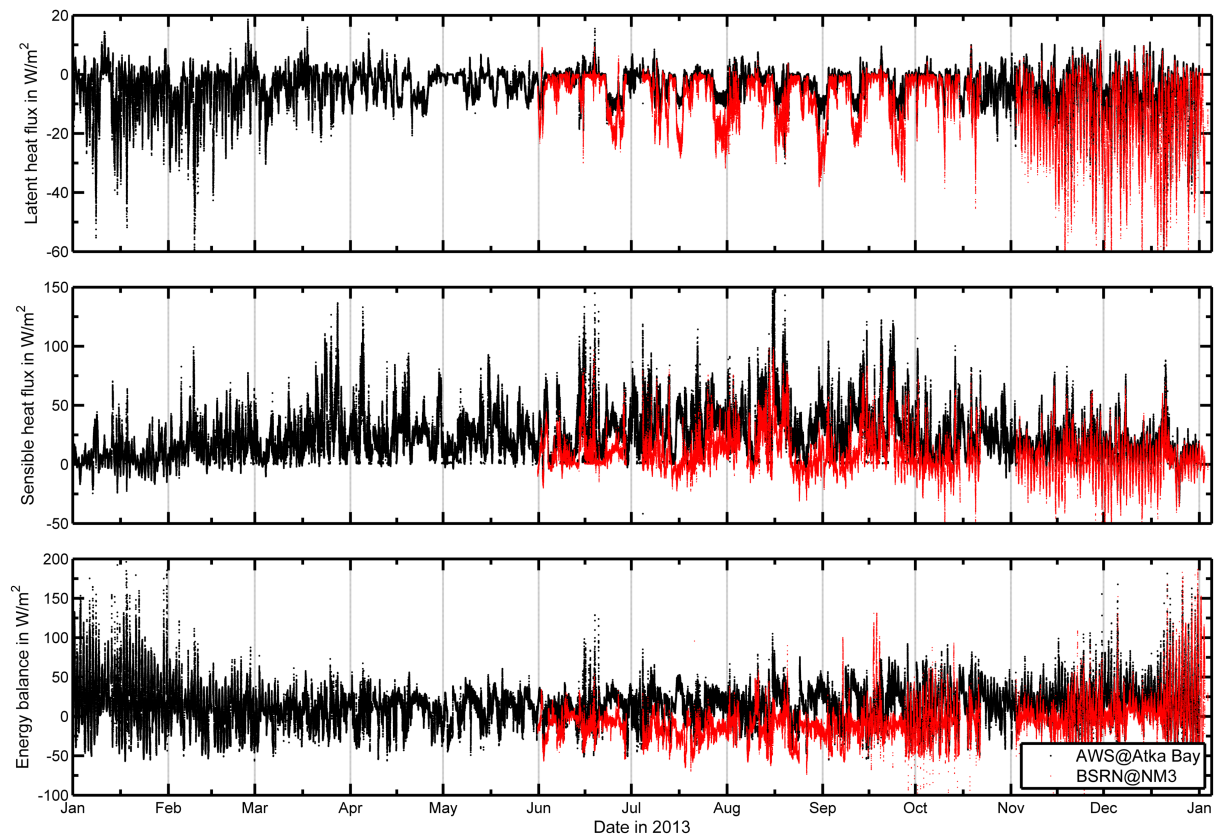


Figure 15: (a) Turbulent flux of latent heat (LH) and b) turbulent flux of sensible heat (SH) measured at Neumayer III (black) and on Atka Bay fast ice (red) in 2013. These were calculated from meteorological measurements, using the Matlab air-sea Toolbox (<http://woodshole.er.usgs.gov/operations/sea-mat/index.html>); c) total energy balance resulting from addition of SWU, SWD, LWU, LWD, SH and LH.

preferred wind direction is easterly, especially between July and October. The strongest winds were the easterlies. The quality of the AWS radiation measurements seems unexpectedly good when taking into account the high standards of the BSRN measurements at Neumayer.

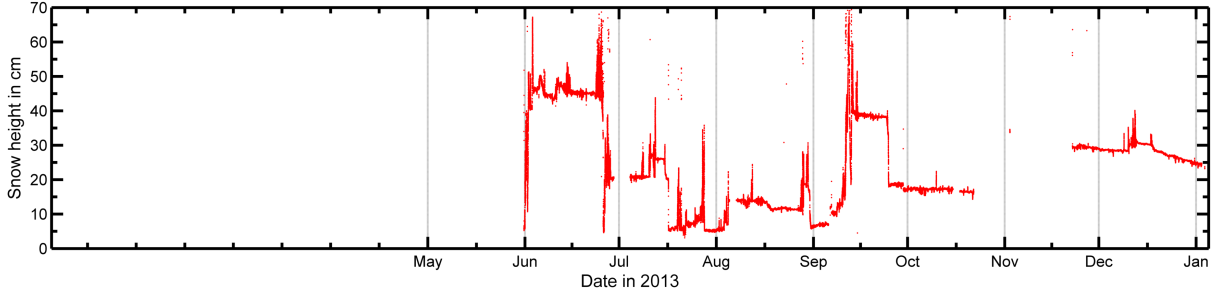


Figure 16: Snow depth at ATKA03, calculated from ultrasonic snow pinger (temperature corrected).

The evolution of the snow cover as measured by the Sonic ranging sensor of the AWS is shown in Figure 16. It is apparent that snow depth was highly variable during the measurement period, recorded values ranging from 0 to 70 cm. The maximal continuous snow depth of 50 cm occurred in June, immediately after deployment. In the following 2.5 months, it varied between 5 and 20 cm, and rises again to 40 cm in mid-September. For the rest of the year it remained between 20 and 30 cm. This dataset will be especially useful when comparing it to the temperature profiles of the IMB described below (not shown here).

4. Radiation station

4.1. 06 September to 11 September 2013

We deployed a spectral radiation station at ATKA03 on 06 September 2013, after a successful test in the station on 02 September. The setup consisted of three RAMSES spectral radiometers measuring incoming spectral irradiance I_{incom} (SAMIP_506B/SAM_8343), reflected irradiance I_{refl} (SAM_8324) and transmitted irradiance through snow I_{transm} (SAMIP_5063/SAM_8328). The latter was deployed in a 10 cm diameter sea-ice core hole, with the head of the sensor at the sea-ice surface. After deployment, the snow cover was restored carefully at the site. The sensors were connected to a Tribox II/Extensionbox powered by 2 lead batteries. Spectra were recorded at 10-minute intervals.

A site a few meters south of the AWS was chosen, in order to be able to deploy the transmittance sensor under a layer of snow. Snow depth at the site of this sensor was 20 cm during deployment, with 10 cm of snow accumulation by drift in the last night alone. The head of the downward-looking sensor had a distance of 0.84 m to the snow surface (Table 4).

A WLAN antenna was attached to the mast of the AWS, pointing in the direction of Neumayer III. This antenna was powered by the solar panels of PALAOA-S, and was only operating during data transfer. Both PALAOA-S and the CR3000 datalogger of the AWS were able to activate

Table 4: Snow depth at sensor sites (RS1)

Date	SAMIP 506B (I_{incom}) Height above snow in cm	SAM 8324 (I_{refl})	SAMIP 5063 Snow depth in cm
20130906	124.5	84	10

the antenna. In addition, the Tribox II of the radiation station was connected to the WLAN switch, making a remote data transfer directly to Neumayer III possible. The Tribox II was also connected to the CR3000 Datalogger of the AWS. The program of the CR3000 was modified to switch off the radiation station after sunset, and switching it on again shortly after sunrise to save power. In addition, the lead batteries were charged by the AWS solar panels. The setup was also configured to be able to control the operation and the charging remotely from the station.

The WLAN antenna was activated by the program of the CR3000 every evening between 21:00 and 21:10 o'clock to retrieve the data. Due to very cold temperatures ($< 30^{\circ}\text{C}$), a data transfer was not always possible. On 17 September, PALAOA-S needed to be retrieved due to problems in the power supply. While the charging of the batteries of the radiation station seemed to work well, no new irradiance data was recorded since 11 September. Although the Tribox II still seemed to be working, the sensor did not record any spectra. After some days of troubleshooting and ruling out the most common problems with the help of the TriOS technical support, two radiometers were retrieved in order to conduct some further testing at Neumayer III. We found that these also did not respond on a manual setup with a PS Box and a PC. As a consequence, we retrieved the other instruments. The third radiometer and the Extension-Box were also not working anymore. It is currently not entirely clear why the instruments failed. However, since the failure happened during a storm with very high wind speeds of more than 25 m/s (see above), we suspect static discharge to be responsible.

As a summary, only 5 days (06 to 11 September) of spectral data were recorded. Thus, the data is not shown here.

4.2. 29 September 2013 to 03 January 2014

On 29 September 2013, a backup system was deployed at the same spot (Figure 17). The setup again consisted of three RAMSES spectral radiometers for incoming spectral irradiance I_{incom} (SAMIP_5058/SAM_82c3), reflected irradiance I_{refl} (SAM_82CE) and transmitted irradiance through snow I_{transm} (SAMIP_505A/SAM_82c0). For the latter, we used the exact same hole in the sea ice as before. The sensors were connected to a backup Tribox II/ Extension-Box powered by 2 lead batteries. This time, the cables were placed into the snow to avoid additional potential static discharge. Spectra were recorded at 10-minute intervals.

Figure 18 shows the recorded spectra for incoming, reflected and transmitted irradiance, while Figure 19 shows the evolution of spectral albedo (I_{refl}/I_{incom}) and transmittance (I_{transm}/I_{incom}) between 29 September 2013 and 03 January 2014. The data gap in October was caused by a

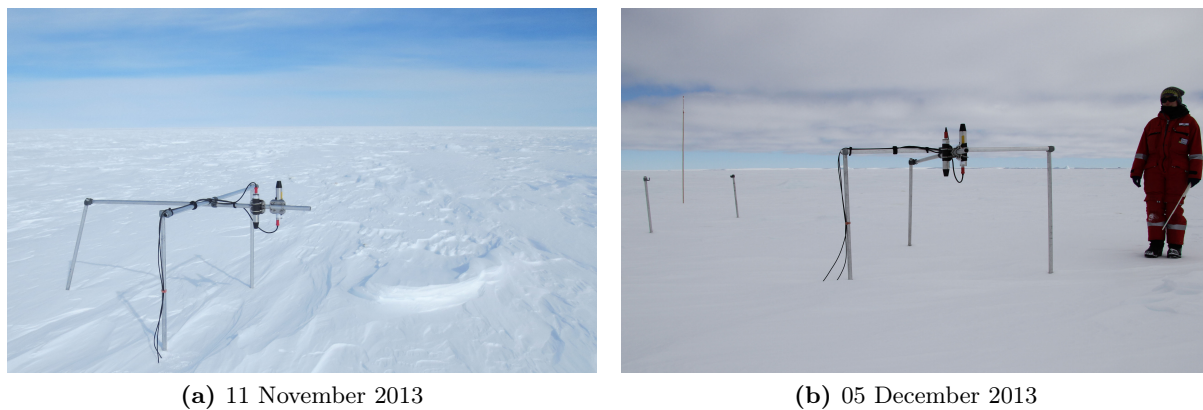


Figure 17: Radiation station

Table 5: Snow depth at sensor sites (RS2)

Date	SAMIP 5058 (I_{incom}) Height above snow in cm	SAM 82CE (I_{refl})	SAMIP 505A (I_{transm}) Snow depth in cm
20130929	124	90	23
20131009	123	90	22.5
20131017	123.5	89	22.5
20131028	120	86	21.5
20131119	109	71	24.5
20131205	110.5	73.5	22.5
20140103	115	78	20

failure in the CR3000 datalogger (see above). Other data gaps were mostly due to power issues, when the lead batteries could not be changed timely because of logistical constraints.

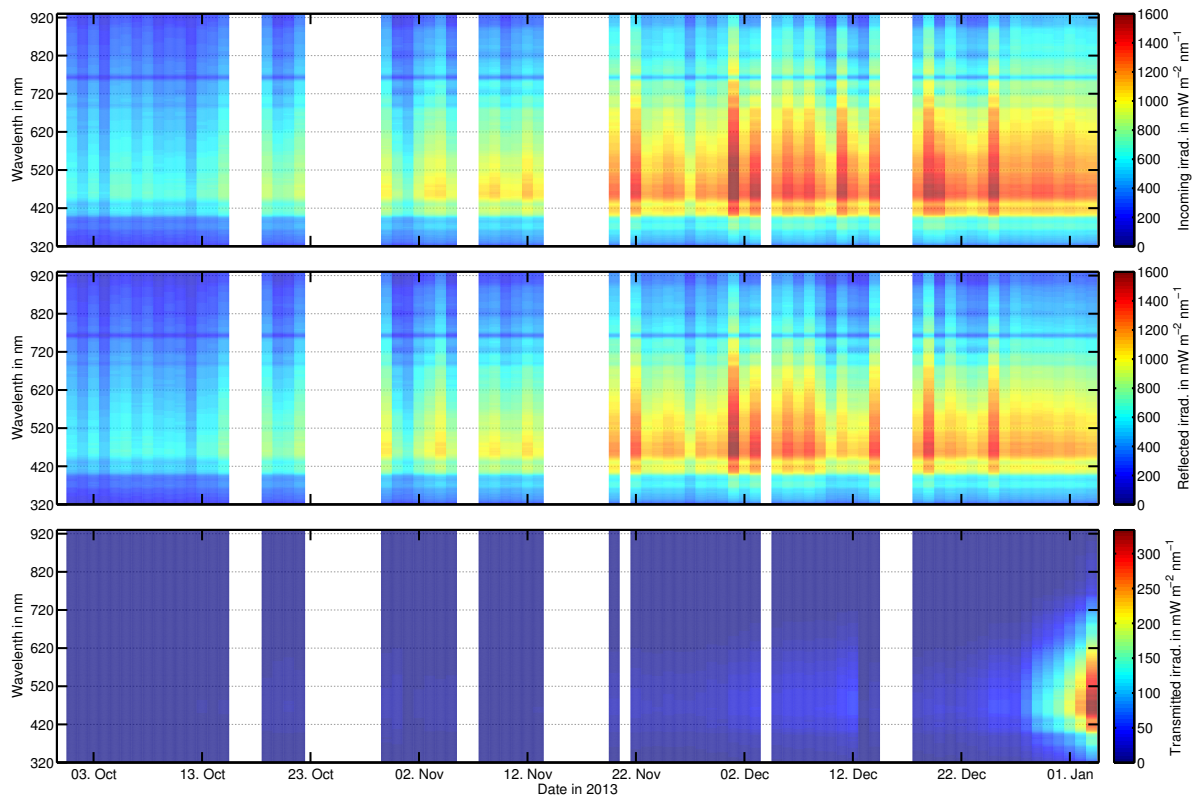


Figure 18: Incoming (top), reflected (middle) and transmitted (bottom) spectral irradiance.

The maximum incoming irradiance was recorded throughout December, as expected. At the end of December 2013, the transmitted irradiance (and also the transmittance) start to increase continuously until the end of the measurements on 03 January 2014. As the snow depth above this sensor only decreased slightly (Table 5), metamorphism processes and an increase in grain size are the most likely explanations. This is also in accordance with the decrease of surface Albedo, although this evolution seems to set in a few days earlier. From the broadband albedo and transmittance (Figure 19) it is evident that the changes occur at the same time, but the increase in transmittance is divided into two distinct periods: first, a period of about 5 days where it increases very slowly, and afterwards a period in which it increases drastically. The “spikes” in the data cannot be explained currently, but it is unlikely that these were measurement errors because they spanned several days.

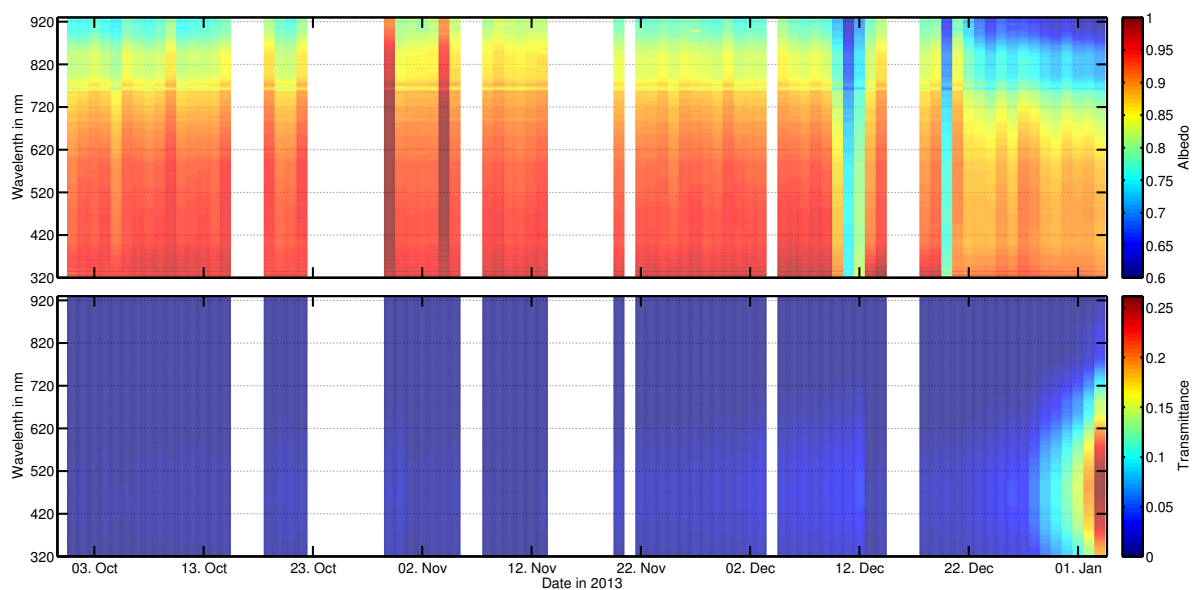


Figure 19: Spectral albedo (top) and transmittance (bottom).

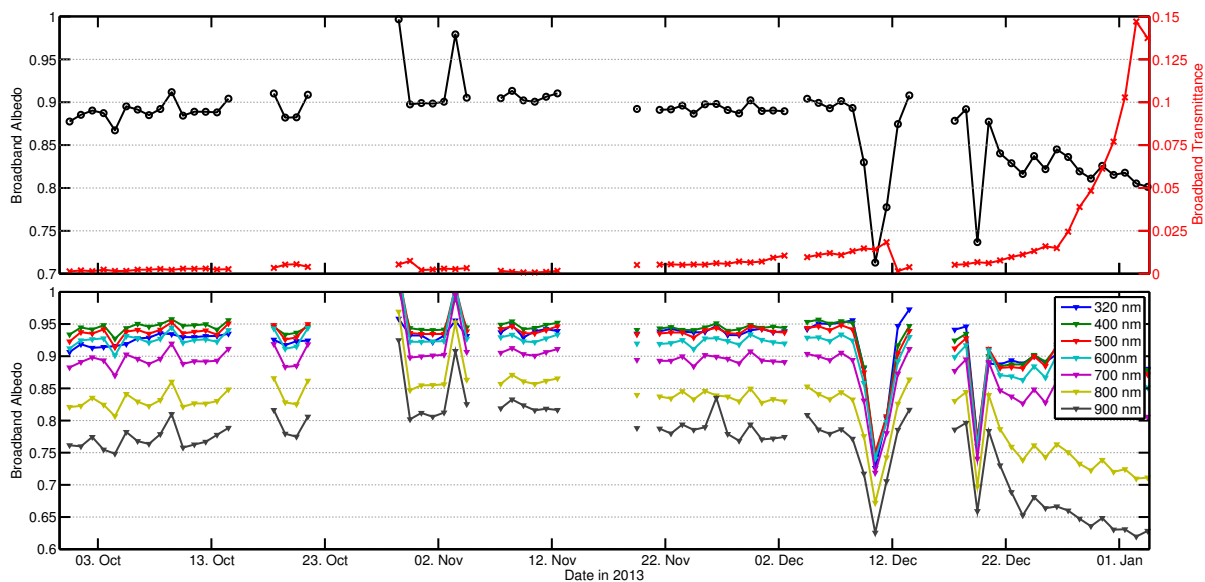


Figure 20: Broadband albedo and transmittance (top) and albedo at selected wavelengths (bottom).

5. Sea-ice mass balance buoy

The sea-ice mass balance buoy AWI31 was frozen into the sea ice on 21 November 2012 at ATKA03. Thickness measurements in the bore-hole yielded an initial sea-ice thickness of 245 cm, a snow depth of 1 cm and a freeboard of about 40 cm. Determination of freeboard was difficult due to masses of ice platelets clogging the borehole. The hole was filled up with snow, but the part above the water surface did not refreeze entirely.

Table 6: Thermistor numbers at interfaces between media

Interface	air/snow	sea ice/snow	sea surface	sea-ice bot.
AWI31	22	22	42	165

Sub-ice platelet-layer thickness was determined as 400 μ m, with several consolidated parts in between. To avoid the floating of the chain in the thick platelet layer, a weight was attached to the end of the chain.

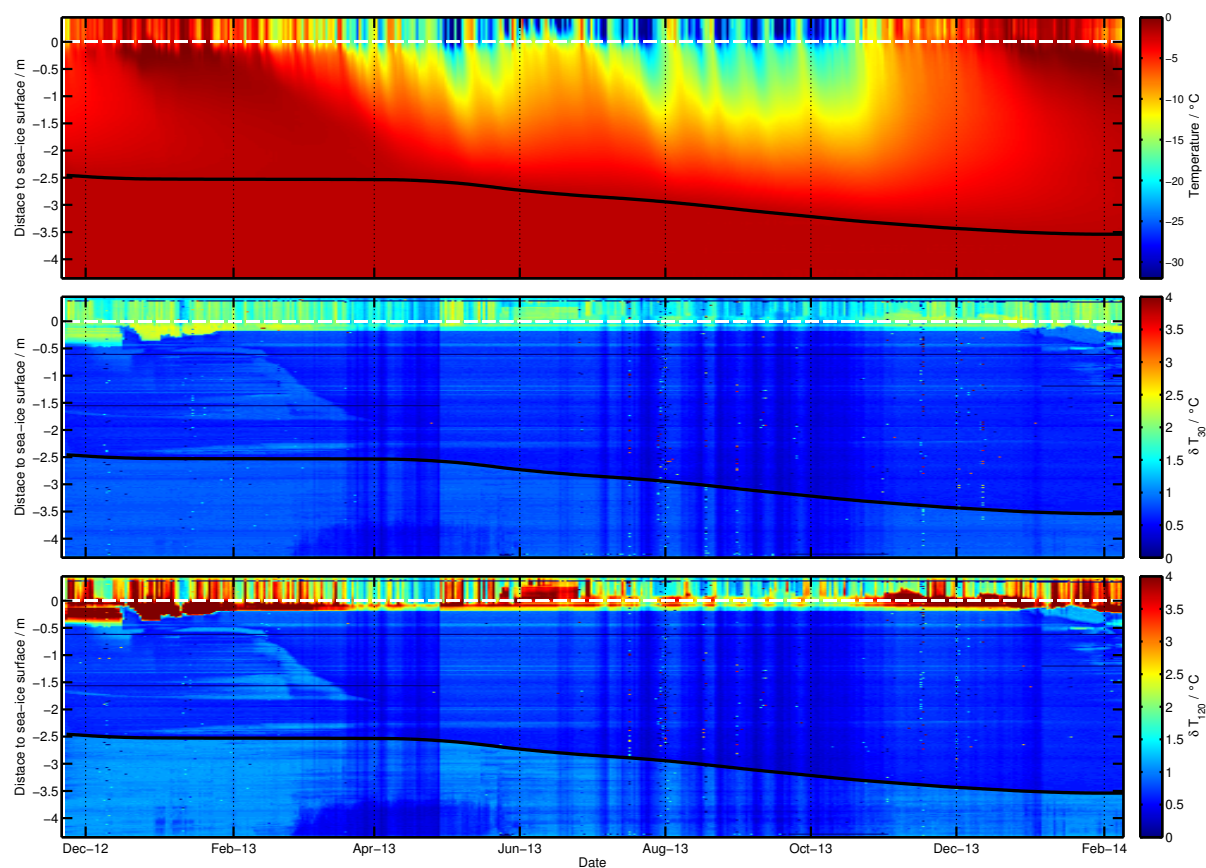


Figure 21: a) Temperature profiles. b) Heating profiles after 30 s. c) Heating profiles after 120 s.

The heating cycle was left at default values of 30 and 120 seconds, with a duty cycle of 100

%. At first, the chain was configured to record data every 6 hours. It was reconfigured to hourly measurements on 11 December 2012 to reveal temperature changes at a higher resolution. During February 2013 the sea ice became nearly isothermal. To save battery life, the measurement interval was set to twice a day since February. The batteries were changed in January 2014 in preparation for a potentially long drift after an expected sea-ice breakout in the following weeks. Unfortunately, the buoy did not survive the breakout in early February, ceasing operation on 09 February 2014. The data shown here was interpolated to a uniform time grid, and each thermistor number was converted to its distance relative to the sea-ice surface based on the conditions during deployment. The temperature data was corrected for misreadings. This procedure is still ongoing with the heating data.

The results of temperature and heating data of IMB AWI31 are provided in Figure 21. The sea-ice bottom is not evident from the temperature data only, especially in isothermal conditions during summer. In contrast, a clear distinction of thermal properties is possible from the heating data, allowing for an accurate determination of the sea-ice/ocean interface. The same applies for the snow cover. As the determination of snow depth is principally possible from temperature data upon close investigation, it is immediately apparent from the heating data. In addition, the internal melt in summer and the progression of the freezing interface during the transition to winter is clearly pronounced in the heating data, and not at all from temperature profiles. The possibility to differentiate the platelet layer from “ordinary” seawater is not assessable with this dataset alone, as the chain was not long enough to reach platelet-free water. The sea ice grew approximately 1 m between 21 November 2013 and 09 February 2014, from 2.5 to 3.5 m. Snow depth was variable, but staying below 0.1 m most of the year. A maximum of nearly 0.5 m occurred in June 2013. One month later, the thick snow then decreased again quickly. A detailed treatment on growth rates, heat fluxes and other information to be derived from the temperature and heating profiles is currently in progress.

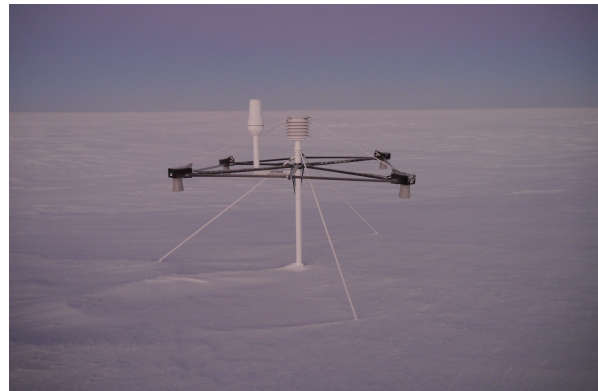
6. Snow buoys

We deployed two newly developed snow buoys (NM_S_002 and NM_S_003) on the ice shelf near Neumayer III on 11 February 2013 (Figure 22). The main aim of this experiment was to test the reliability of those prototypes under “real” Antarctic conditions. A location near the air chemistry observatory was chosen as a test site, because our colleagues had already mounted another snow height sensor on a nearby mast.

At the beginning of April 2013, one of the four ultrasonic pinger of NM_S_002 had a failure. On 30 April 2013, the three others also had malfunctions. Air temperature and barometric pressure were still recorded and sent via satellite as usual. The buoy was retrieved on 08 May 2013 and examined closer at Neumayer. A failure of a multiplexer on a small auxiliary circuit board could be identified, while the four snow pinger themselves were still functional. The failure of the multiplexer was assumed to originate from static discharge, because the electronics were generally not properly connected to the housing. At the same time, an unusual behaviour of at



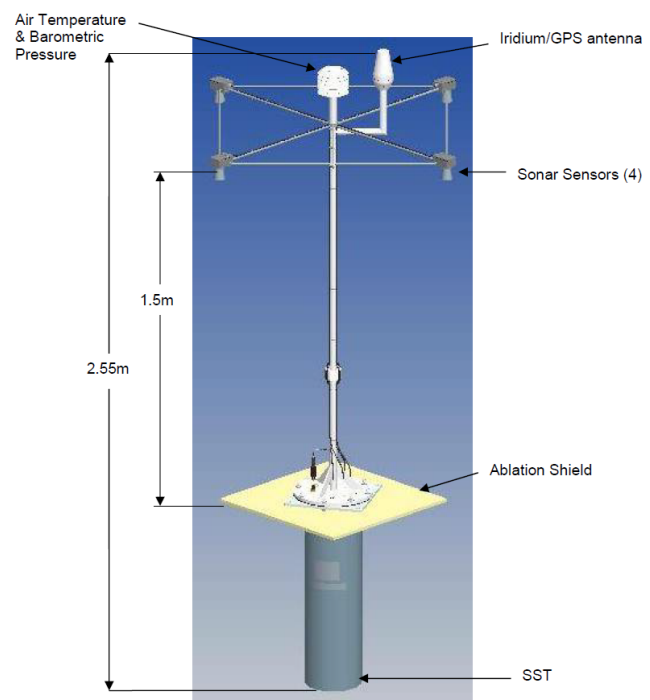
(a) 11 February 2013



(b) 05 July 2013



(c) 15 August 2013



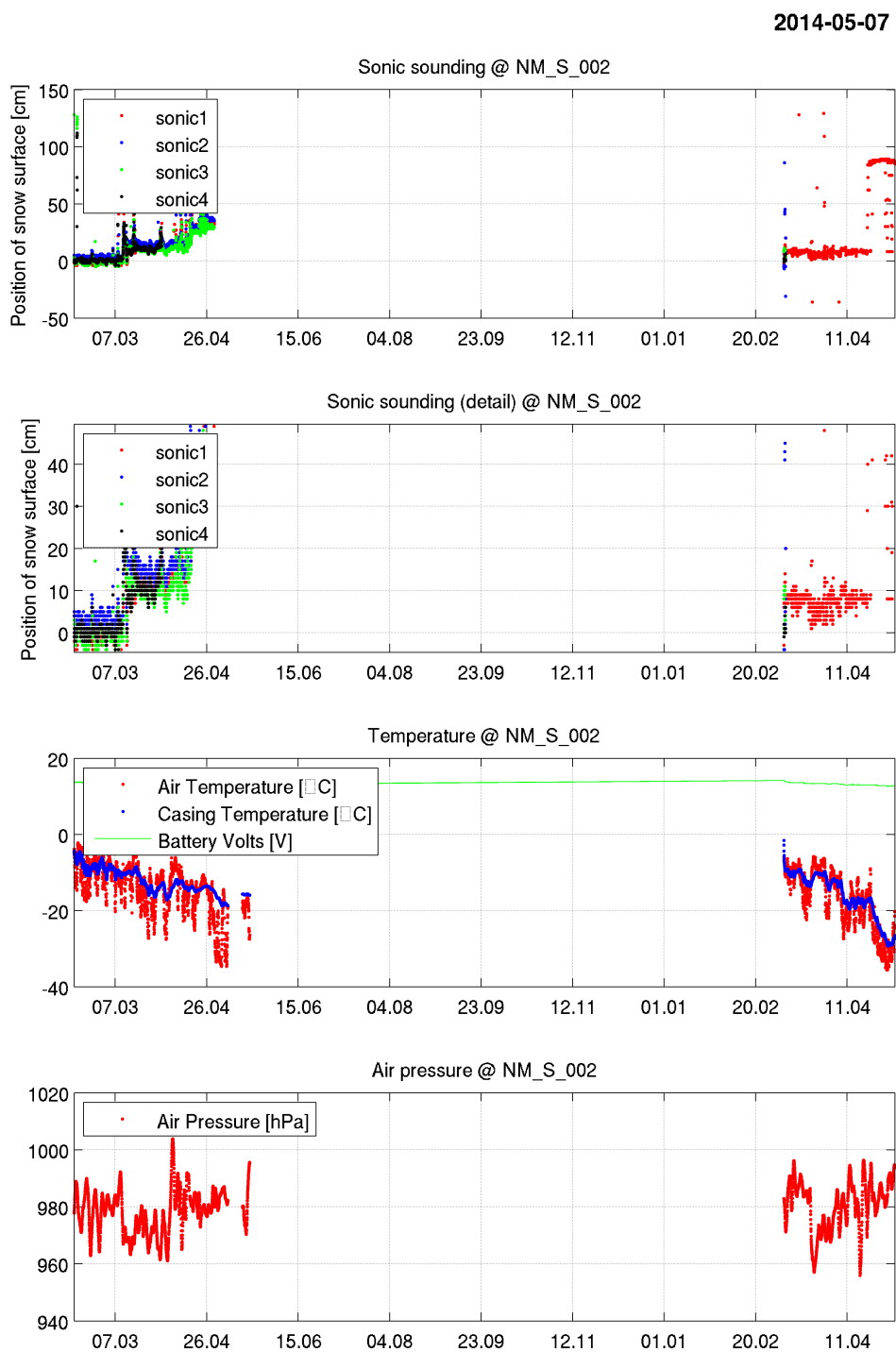
(d) Scheme (MetOcean)

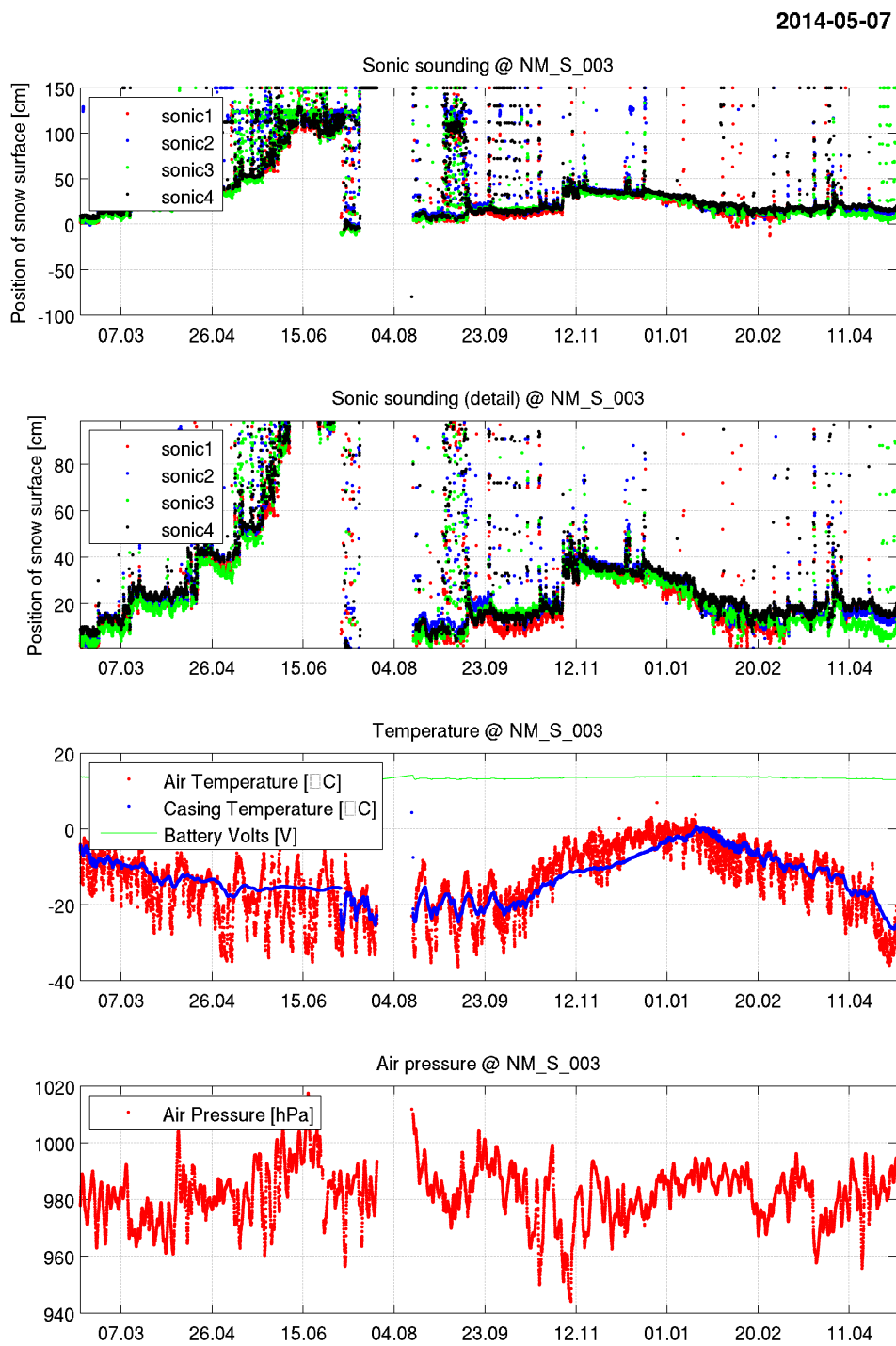
Figure 22: Snow buoy

least two snow pingers of NM_S_003 was observed during periods of temperatures < 30 °C. However, this buoy was left in the field to find out if the total failure of the other buoy was a general issue. Due to a large snow accumulation, NM_S_003 was ramped up to the snow surface on 05 July 2013 (Figure 22).

On 16 July 2013, the same symptoms of failure also occurred with NM_S_003. The buoy was retrieved and parts from NM_S_002 were used to repair it, along with several modifications of the electronics. A detailed description of those modifications is out of the scope of this report. NM_S_003 was again deployed outside the station on 15 August 2013 (Figure 22). The troubleshooting was done in cooperation with MetOcean, who subsequently overworked the concept. Spare parts were shipped to Neumayer in December in order to test this modification. NM_S_002 was repaired and re-deployed on 07 March 2014. Shortly afterwards, 3 of the 4 snow pingers again stopped sending data. At the time of writing, the buoy is retrieved and checked for malfunctions.

The time-series of both snow buoys are presented in Figures 23 and 24. These data shall not be discussed here in more detail.

**Figure 23:** Snow buoy NM_S_002

**Figure 24:** Snow buoy NM_S_003

A. Acknowledgements

The authors are most grateful to the Neumayer III overwintering teams in 2013 and 2014 for their support in the field. In addition, René Fontes contributed significantly to the troubleshooting and subsequent improvement of the snow buoys. We thank the German Space Agency (DLR) for the TerraSAR-X image. We highly acknowledge Gert König-Langlo and Holger Schmithüsen for their help with the meteorological data, and Bernd Loose for his technical support. We express our gratitude towards Lars Kindermann for the CTD data. Our research at Neumayer III would not have been possible without the support of the AWI logistics. This work was supported by the German Research Council (DFG) in the framework of the priority programme “Antarctic Research with comparative investigations in Arctic ice areas” by grants to SPP1158, NI 1092/2 and HE2740/12, and the Alfred-Wegener-Institut Helmholtz-Zentrum für Polar- und Meeresforschung.